Investigation of a turbulent boundary layer flow at high Reynolds number using particle-imaging and implications for RANS modeling

Tobias Knopp

Institute of Aerodynamics and Flow Technology
German Aerospace Center (DLR)
Bunsenstr. 10, 37073 Göttingen, Germany
Tobias.Knopp@dlr.de

Nico Reuther

Institute for Fluid Mechanics and Aerodynamics
Universität der Bundeswehr München (UniBw)
Werner-Heisenberg-Weg 39, 85577 Neubiberg, Germany
Nico Reuther@unibw.de

M. Novara, E. Schülein, D. Schanz, A. Schröder

Institute of Aerodynamics and Flow Technology
German Aerospace Center (DLR)
Bunsenstr. 10, 37073 Göttingen, Germany
Matteo.Novara@dlr.de, Erich.Schuelein@dlr.de
Daniel.Schanz@dlr.de, Andreas.Schroeder@dlr.de

Christian J. Kähler

Institute for Fluid Mechanics and Aerodynamics
Universität der Bundeswehr München (UniBw)
Werner-Heisenberg-Weg 39, 85577 Neubiberg, Germany
Christian.Kaehler@unibw.de

INTRODUCTION

The prediction of pressure induced separation of a turbulent boundary layer (TBL) subjected to an adverse pressure gradient (APG) in the subsonic regime using RANS-based CFD is still associated with significant uncertainties. We present a new experiment of a TBL at APG at large Re_θ. The design includes lessons learned from a precursor experiment Knopp *et al.* (2015). Some preliminary results were shown in Knopp & Reuther (2015) and Reuther *et al.* (2015). The goals of the experiment are (i) to enrich the data base of mean velocity and Reynolds stress profiles for TBL at APG, (ii) to propose an empirical wall law at APG for the inner layer using the data base, (iii) to establish a well defined test case for the validation of RANS turbulence models, and (iv) to improve RANS models. This experiment complements other recent studies on TBL at APG, which are both experimentally, e.g., within the EU project EuHIT (see https://www.euhit.org/), and numerically, e.g. in Gungor *et al.* (2016) and Kitsios *et al.* (2016).

EXPERIMENTAL SETUP

We performed the new experiment in the Eiffel type atmospheric wind tunnel of UniBw in Munich, which has a 22 m long test section with a rectangular cross section of $2 \times 2\,\mathrm{m}^2$.

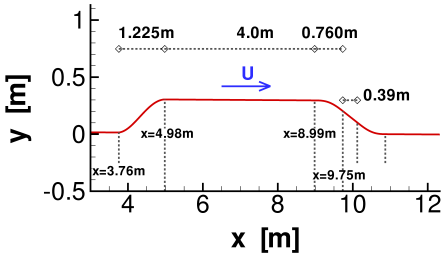

Figure 1. Sketch of the wind tunnel experiment with flow direction (axes not to scale).

The flow develops on the wind tunnel wall over 4.26 m and then reaches the geometry model, which is sketched in Figure 1. The flow is accelerated along a first ramp of height 0.30 m and of length 1.225 m and then relaxes along a flat plate of length 4.0 m at almost zero pressure gradient (ZPG) towards equilibrium. Then the flow follows a curvilinear deflection of length 0.75 m which initially causes a small favourable pressure gradient (FPG), and then enters into the APG region at $x > 9.42$ m, see Reuther *et al.* (2015). The focus region is over an inclined flat plate of length 0.4 m at an opening angle of 14.4°. The opening angle was chosen to keep the flow remote from separation based on CFD results with the DLR TAU code using the Spalart-Allmaras (SA) model and the Menter SST k-ω model. Finally, the flow follows a second deflection which brings the flow down to the wind tunnel wall again.

The experiments were performed at a free-stream velocity of $U_\infty = 10\,\mathrm{m/s}$, $U_\infty = 23\,\mathrm{m/s}$, and $U_\infty = 36\,\mathrm{m/s}$ measured at the inlet of the test section, yielding $Re_\theta = 8400$, 16000, and 23000 at $x = 8.36$ m in the ZPG region and $Re_\theta = 15000$, 28000, and 41000 at $x = 9.94$ m in the adverse pressure gradient region.

MEASUREMENT TECHNIQUE

Different tracer particle based field measurement approaches were combined to match the goal of measuring the mean velocity and the Reynolds stresses over a large streamwise extent of $15\delta_{\mathrm{ref}}$ from the outer edge of the boundary layer down to the viscous sublayer, with δ_{ref} being the boundary layer thickness $\delta_{995} = 0.16$ m at $x = 8.12$ m. For an overview measurement from $x = 8$ m to $x = 10.23$ m we applied a multi-camera large-scale particle image velocimetry (2D2C-PIV) measurement using 9 cameras side by side for the two velocity components (2C) in streamwise and wall-normal direction in a 2D plane. These data sets were evaluated using a single pixel and a window correlation method, see Reuther *et al.* (2015) and resolve a large part of the inner layer down to e.g., $y^+ = 60$ for $U_\infty = 10\mathrm{m/s}$. The mean velocity profiles and Reynolds stresses were extracted at 13 streamwise positions.

High resolution measurements were performed in the APG region on the inclined flat plate. A high magnification approach using long-range microscopic particle tracking velocimetry (2D-μPTV) by Kähler *et al.* (2012) was applied to remedy the low spatial resolution posed by the finite size of the interrogation window. The near-wall field of view was $20 \times 17\,\mathrm{mm}^2$ with reliable data points down to $y^+ = 1.5$ for $U_\infty = 10\mathrm{m/s}$. Additionally we used the new Shake-The-Box (STB) 3D-PTV approach for $U_\infty = 36\mathrm{m/s}$ which was applied here in a multi-pulse acquisition strategy, see Novara

et al. (2016). The macroscopic field of view of $50 \times 90 \times 8\,\mathrm{mm}^3$ covered half the boundary-layer thickness. For $U_\infty = 10\,\mathrm{m/s}$ we applied Tomo-PIV using the same macroscopic field of view. Using the 3D3C approaches, the full Reynolds stress tensor is measured.

The wall shear stress τ_w was determined from the 2D2C-PIV data using the standard Clauser chart method (CCM). Additionally τ_w was determined directly from the viscous sublayer profiles of the 2D-μPTV data at one position in the APG region. Oil-film interferometry (OFI) was used during a repetition of the measurements, Schülein *et al.* (2017). During the OFI measurements, the kinematic viscosity ν was higher by around 10% in the Eiffel type wind tunnel compared to the PIV campaign due to different weather conditions in winter and summer, and U_∞ was kept constant.

CHARACTERIZATION OF THE FLOW

To characterize the flow along the region of interest, we study the streamwise pressure gradient. We use the inner scaling Δp_x^+ for the inner part of the boundary layer, and the Zaragola-Smits scaling β_{ZS} for the outer part of the boundary layer, see Figure 2. On the 0.75m long curvilinear deflection, both the inner and the outer part of the boundary layer first experience an FPG, and then, for $x >$ 9.3m, an APG. Interestingly, $\Delta p_x^+ = \nu/(\rho u_\tau^3)\mathrm{d}P/\mathrm{d}x$ is increasing on both the curvilinear element and the inclined flat plate ($9.75\mathrm{m} < x <$ 10.14m), whereas β_{ZS} reaches a maximum at around $x = 9.65$m, then decreases and remains roughly constant for $x > 9.8$m.

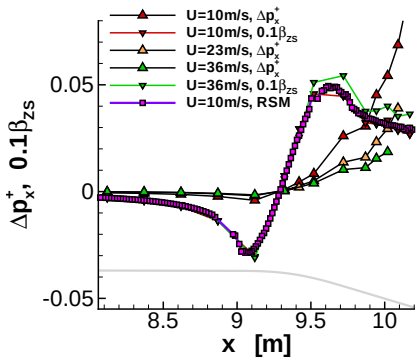

Figure 2. Pressure gradient parameters along the contour.

Along the curvilinear deflection, the ratio of the boundary layer thickness δ_{99} to the radius of curvature of the wall R_w is up to 0.012, from which we can expect significant effects of mild surface curvature, see e.g. Ramaprian & Shivaprasad (1978).

MEAN VELOCITY AT APG

In the APG region, we observe a small layer, where the mean velocity profile can be fitted to a log-law (see Figure 3)

$$u^+ = \frac{1}{K_i}\log(y^+) + B_i \tag{1}$$

This region is thin and extends from $y^+ = 80$ to $y^+ = 160$ at $x =$ 9.94m for $U_\infty = 36\,\mathrm{m/s}$, where $\Delta p_x^+ = 0.015$. The log-law slope diagnostic function Ξ^{-1}, with $\Xi = y^+\mathrm{d}u^+/\mathrm{d}y^+$, is plotted for the 3D PTV STB data in Figure 4 and shows a small plateau in this region.

We determine K_i by log-linear regression. We observe that K_i is smaller than for ZPG TBL and decreases with increasing Δp_x^+,

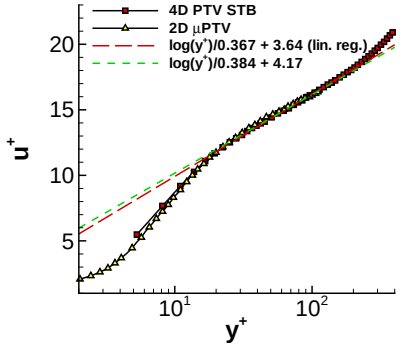

Figure 3. u^+ vs. y^+ at $x = 9.94$m and $U_\infty = 36$m.

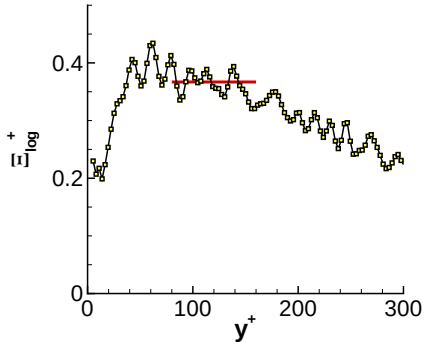

Figure 4. Log-law diagnostic function at $x = 9.94$m, $U_\infty = 36$m.

supporting the work by Nickels (2004), see Figure 5. Therein u_τ is computed from the Clauser chart method (CCM) or from a linear fit in the viscous sublayer (direct). Regarding the intercept B_i, the values for $K_i B_i$ are plotted against B_i in Figure 6 and follow the correlation proposed by Nagib & Chauhan (2008).

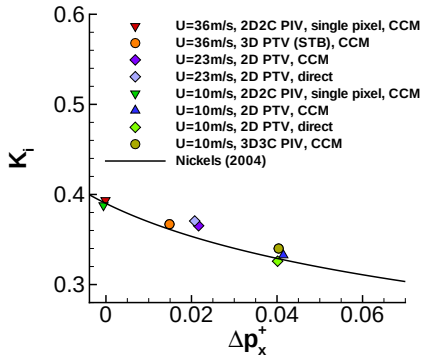

Figure 5. Log-law slope K_i vs. Δp_x^+.

A half-power law (or: sqrt-law) region beyond the log-law region is proposed by some authors, e.g. Perry (1966)

$$u^+ = \frac{1}{K_o}\log(y^+) + \frac{2}{K_o}\left(\sqrt{1+\Delta p_x^+ y^+} - 1\right) + \frac{2}{K_o}\log\left(\frac{2}{\sqrt{1+\Delta p_x^+ y^+}+1}\right) + B_o \tag{2}$$

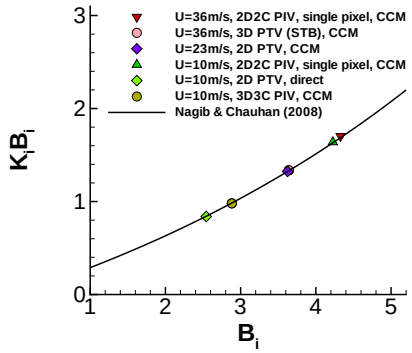

Figure 6. Log-law slope K_i and intercept B_i.

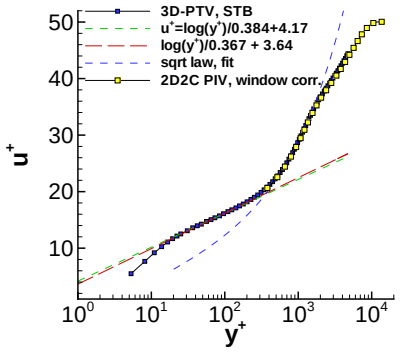

Figure 7. Composite profile and sqrt-law region for $U = 36\,\mathrm{m/s}$.

A fit of (2) to the 3D PTV STB data is shown in Figure 7. The corresponding generalized mean velocity slope diagnostic function is $\Xi_{\mathrm{sqrt}} = y^+/\sqrt{\tau^+(y^+)}\mathrm{d}u^+/\mathrm{d}y^+ = 1/K_o$ with shear stress τ. For the choice $\tau^+ = 1 + \Delta p_x^+ y^+$ approximately a plateau is obtained for $600 < y^+ < 0.1\delta_{99}^+$, see Figure 8. A theoretical reasoning for this cannot be found, since a linear form for τ is not found in this region. For the purpose of improving RANS models, the assumption of a sqrt-law model is helpful and simplifies theoretical reasoning.

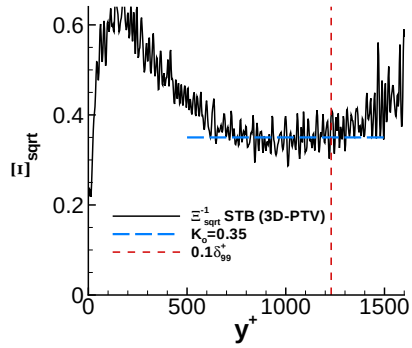

Figure 8. Slope diagnostic function of the sqrt-law.

The slope coefficient K_o can be determined by a least-square fit of (2) to the data, which is plotted in Figure 9. Therein the 2D2C-PIV data might be effected by an additional uncertainty due to the indirect Clauser chart method used for u_τ.

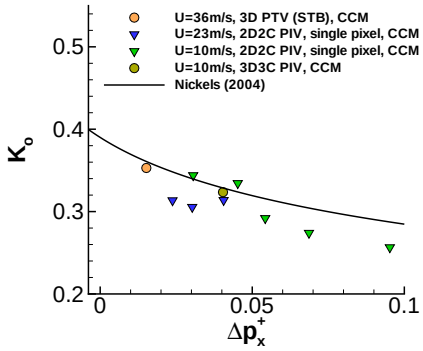

Figure 9. Sqrt-law slope K_o vs. Δp_x^+.

Then we aim to relate the extent of the log-law region $y^+_{\mathrm{log,max}}$ and the begin of the sqrt-law region $y^+_{\mathrm{sqrt,min}}$ to a suitable flow parameter. We use a literature data base and the present data. For each velocity profile u^+ we determine the y^+-value where the upward turn of the velocity profile above the log-law (1), i.e. $\Delta u^+ \equiv u^+ - \log(y^+)/K_i - B_i$, becomes significant. We attempt a simple model by relating $y^+_{\mathrm{log,max}}$ and $y^+_{\mathrm{sqrt,min}}$ to Δp_x^+ and propose

$$y^+_{\mathrm{log,max}} = 64(\Delta p_x^+)^{-0.35}, \quad y^+_{\mathrm{sqrt,min}} = 110(\Delta p_x^+)^{-0.35} \qquad (3)$$

The result for $y^+_{\mathrm{log,max}}$ is shown in Figure 10.

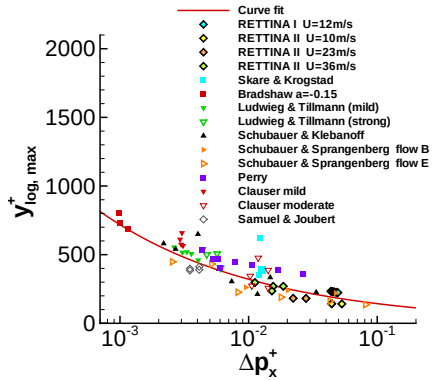

Figure 10. Extent of the log-law region at APG.

RESULTS FOR THE REYNOLDS STRESSES

In order to assess the accuracy of the 2D2C-PIV measurement technique, we first consider the results for $x = 8.12\,\mathrm{m}$, where the flow is almost at ZPG. We compare the results with hot-wire data at similar values for Re_θ from the literature for $U_\infty = 10\,\mathrm{m/s}$ in Figure 11. The resolution of the 2D2C-PIV technique is assessed to be good for quantitative statements for $U_\infty = 10\,\mathrm{m/s}$ and satisfying for qualitative conclusions for $U_\infty = 36\,\mathrm{m/s}$.

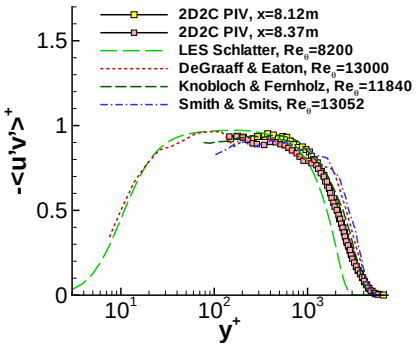

Figure 11. $\overline{u'v'}$ at almost ZPG at $x = 8.12\,\mathrm{m}$ for $U = 10\mathrm{m/s}$.

The streamwise evolution of the Reynolds stresses for $U_\infty = 10\,\mathrm{m/s}$ is shown in Figures 12-14. The streamwise component $\overline{u'^2}$ is moderately altered in the curvature region ($x = 9.32$m, $x = 9.52$m), where $\overline{u'^2}$ is reduced for $y < 0.5\delta_{99}$ and little increased for $y > 0.5\delta_{99}$. In the APG region ($x = 9.94$m), $\overline{u'^2}$ is increased significantly for $y < 0.2\delta_{99}$. The wall-normal component $\overline{v'^2}$ is significantly reduced in the curvature region ($x = 9.32$m, $x = 9.52$m) for $y < 0.5\delta_{99}$ and little altered in the outer part for $y > 0.5\delta_{99}$. In the APG region ($x = 9.94$m), $\overline{v'^2}$ is increased for $y < 0.2\delta_{99}$.

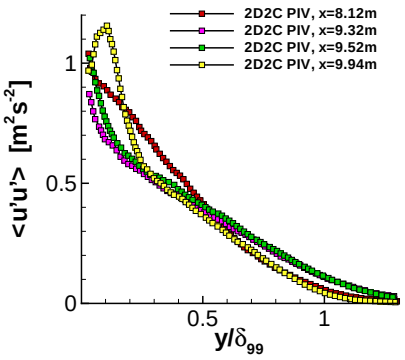

Figure 12. Streamwise evolution of $\overline{u'^2}$ for $U = 10\,\mathrm{m/s}$.

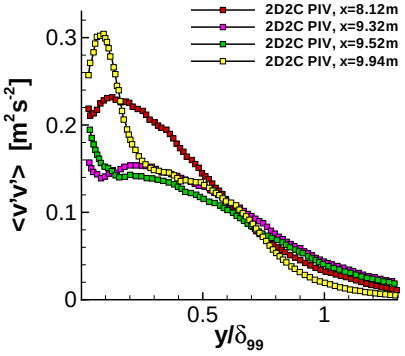

Figure 13. Streamwise evolution of $\overline{v'^2}$ for $U = 10\,\mathrm{m/s}$.

The shear-stress component $-\overline{u'v'}$ is strongly altered in the curvature region ($x = 9.32$m, $x = 9.52$m). At $x = 9.32$m, its magnitude is significantly reduced for $y < 0.6\delta_{99}$. At $x = 9.52$m, its level is further reduced in the entire boundary layer except for $y < 0.1\delta_{99}$. The quantitative effect is comparable with the mild curvature flow results in Ramaprian & Shivaprasad (1978) at $\delta_{99}/R_w = 0.01$, and stronger than reported for the flow by Gibson *et al.* (1984). In the APG region ($x = 9.94$m), $-\overline{u'v'}$ is increased for $y/\delta_{99} < 0.15$ and reaches values larger than for the ZPG position ($x = 8.12$m). We assume that this increase is caused by the APG, since it is qualitatively much larger than the increase observed for turbulent boundary layer relaxation from convex curvature during the initial recovery reported by Alving *et al.* (1990). Interestingly, $-\overline{u'v'}$ remains small in the outer part of the boundary layer.

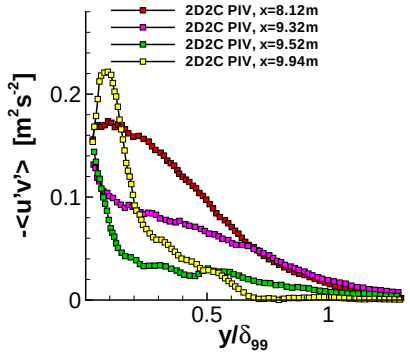

Figure 14. Streamwise evolution of $-\overline{u'v'}$ for $U = 10\,\mathrm{m/s}$.

The correlation coefficient $-\overline{u'v'}/(u_{\mathrm{rms}}v_{\mathrm{rms}})$ with $u^2_{\mathrm{rms}} = \overline{u'^2}$ and $v^2_{\mathrm{rms}} = \overline{v'^2}$ is plotted in Figure 15. In the region of curvature, the turbulence becomes significantly less correlated for $y > 0.1\delta_{99}$ in streamwise direction. In the APG region ($x = 9.94$m) on the flat plate element, the correlation coefficient seems to recover to the ZPG value (at $x = 8.12$m) in the inner layer $y < 0.15\delta_{99}$. It is increasing very slowly for $y < 0.5\delta_{99}$ and is continuing to decrease for $y > 0.5\delta_{99}$. A reduction of $-\overline{u'v'}/(u_{\mathrm{rms}}v_{\mathrm{rms}})$ is reported for the non-equilibrium APG flow in Gungor *et al.* (2016).

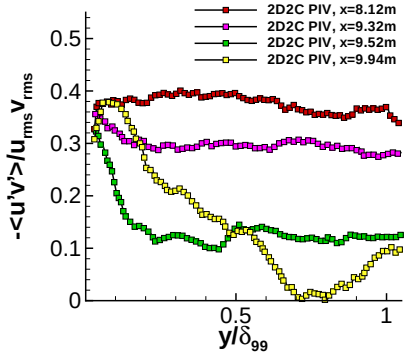

Figure 15. Evolution of $-\overline{u'v'}/(u_{\mathrm{rms}}v_{\mathrm{rms}})$ for $U = 10\,\mathrm{m/s}$.

For the Bradshaw anisotropy ratio $a_{12} = |\overline{u'v'}|/k$ with $k = 0.5(\overline{u'^2} + \overline{v'^2} + \overline{w'^2})$ we find a maximum value of $a_{12} = 0.207$ in the APG region ($x = 9.94$m) for the 3D PTV STB data for $U_\infty = 36\,\mathrm{m/s}$, which is lower than the values found for TBL at ZPG.

CURVATURE AND HISTORY EFFECTS

In the curvature region $8.99\,\mathrm{m} < x < 9.75\,\mathrm{m}$, we assume that the flow is not in equilibrium. An indication for this is the reduction of the correlation coefficient. Another aspect is that the mean velocity profiles in the inner part of the boundary layer are altered and differ from the universal log-law. In Figure 16 we use OFI for determining u_τ. Moreover, the deviation between CCM and OFI is largest in this region, albeit, when comparing CCM and OFI, the 10% smaller *Re* values of the OFI campaign need to be mentioned. The non-equilibrium could be caused by the mild curvature, the radial pressure gradients (which lead to effects involving higher order boundary layer approximations), or the change from FPG to APG and large values of $\mathrm{d}\beta_{ZS}/\mathrm{d}x$ for $9.15\,\mathrm{m} < x < 9.5\,\mathrm{m}$.

On the inclined flat plate for $x > 9.75\,\mathrm{m}$, the relaxation of curvature is superimposed by the APG. The separation of the effects is attempted by considering the eddy turnover time $\tau_{\mathrm{t.o.}} = \kappa_0 * y/|\overline{u'v'}|^{1/2}$ with $\kappa_0 = 0.41$. The turnover length $\delta_{\mathrm{t.o.}} = U\tau_{\mathrm{t.o.}}$ is the corresponding streamwise traveling distance of the local mean flow $U(y)$ see Siliero *et al.* (2013). It is plotted in Figure 17 for $U_\infty = 10\,\mathrm{m/s}$. Regarding the inner layer $y < 0.15\delta_{99}$, the flow is assumed to relax to equilibrium after $2\tau_{\mathrm{t.o.}}$, corresponding to $4\delta_{\mathrm{ref}}$, which corresponds to the mid of the inclined flat plate. Indeed we observe a recovery of the log-law region for $x \geq 9.94\,\mathrm{m}$.

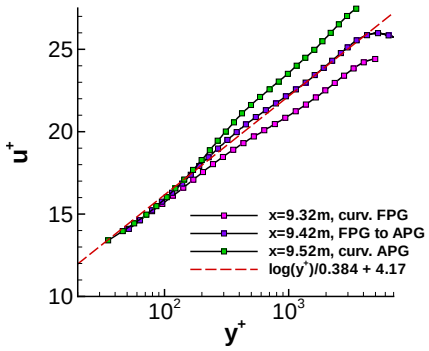

Figure 16. Curvature region, $U = 10\,\mathrm{m/s}$. u^+ vs. y^+ using OFI.

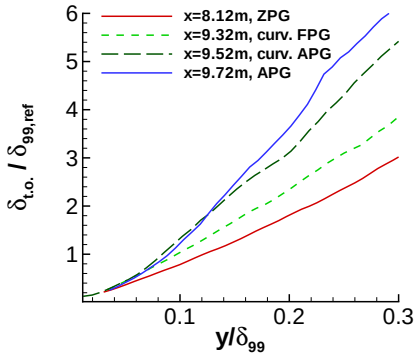

Figure 17. Estimation of history effects using the turnover length.

VALIDATION OF RANS MODELS

The test case is well-defined and used to validate some advanced RANS turbulence models. Here the case is simulated as a 2D flow. We focus on two differential Reynolds stress models (RSM), the SSG/LRR-ω RSM by Eisfeld and the (homogeneous) ε^h-based JHh-v2 model, both documented in Cecora *et al.* (2015). The mean velocity profiles predicted by these models show small differences already in the ZPG region and remarkable differences in the region of curvature and in the APG region on the inclined flat plate. These differences are mainly caused by the length scale equation, whereas the changes due to redistribution and turbulent transport are much smaller. The exact equation for ω derived from the equation for ε (see Wilcox (1998)), adopted for RSM, reads

$$\vec{U}\cdot\vec{\nabla}\omega = \frac{\alpha}{\nu_t}P_k - \beta_\omega\omega^2 + \vec{\nabla}\cdot\left(\left(\nu + \frac{\nu_t}{\sigma_\omega}\right)\vec{\nabla}\omega\right) + D_{\omega,cd} + D_{\omega,dk} \tag{4}$$

with production term P_k, $k = \overline{u_i'u_i'}/2$, $\nu_t = k/\omega$, and the following cross-diffusion term $D_{\omega,cd}$ and additional diffusion term $D_{\omega,dk}$

$$D_{\omega,cd} = c_{d,1}\frac{1}{\omega}\vec{\nabla}k\cdot\vec{\nabla}\omega\,, \quad D_{\omega,dk} = c_{d,2}\left(\vec{\nabla}^2 k + \frac{1}{k}\vec{\nabla}k\cdot\vec{\nabla}k\right) \tag{5}$$

In the SSG/LRR-ω model, $\max(D_{\omega,cd}, 0)$ is used and $D_{\omega,dk}$ is omitted. From the c_f-distribution shown in Figure 18, we see that in the FPG region the near-wall velocity is reduced stronger for the JHh-v2 model than for the SSG/LRR-ω model. The mean velocity at $x = 9.94\,\mathrm{m}$ in the APG region shows a good agreement in dimensional units for the JHh-v2 model, see Figure 19.

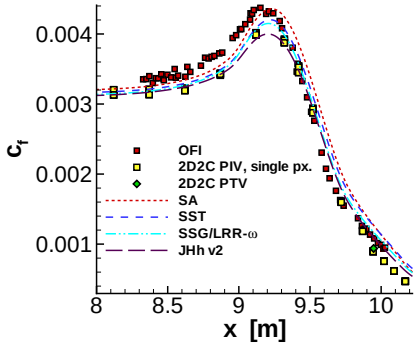

Figure 18. $U_\infty = 36\,\mathrm{m/s}$: streamwise distribution of c_f.

The plot u^+ vs. y^+ in Figure 20 shows the potential of all models for improvement. SST and SSG/LRR-ω give a good agreement with the log-law, but underpredict the slope in the supposed sqrt-law region. The JHh-v2 model could be improved regarding the log-law intercept at APG.

Finally the question of "asymptotically high *Re*" is raised regarding the supposed sqrt-law at APG and the behaviour of RANS models. As an illustration Figure 21 shows Ξ_{sqrt} for the mean velocity on the upper side of the HGR01 airfoil at high $Re_c = 25\times10^6$ based on the chord c, $Ma = 0.15$ and $\alpha = 10^\circ$ near the trailing edge where the flow is attached and remote from separation at $\Delta p_x^+ \approx 0.003$. The extent of the proposed sqrt-law region is increased compared to the present experiment, see Figure 8. All models are far from a plateau in the proposed sqrt-law region given by (3). This indicates that *Re* in the experiment still needs to be increased from the viewpoint of RANS modelling.

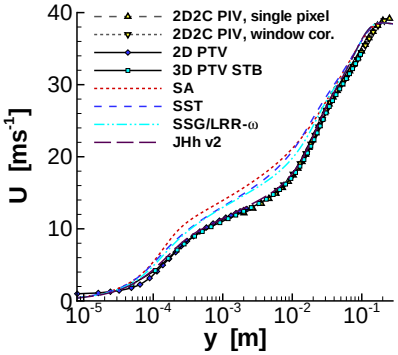

Figure 19. u^+ vs. y^+ for $U_\infty = 36\,\mathrm{m/s}$ at $x = 9.94\,\mathrm{m}$.

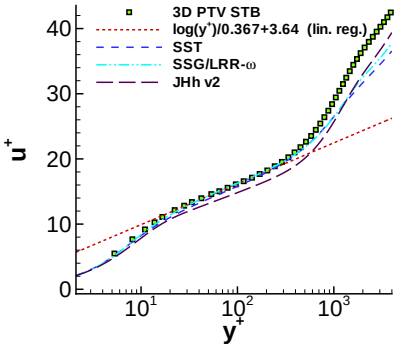

Figure 20. Mean velocity for $U_\infty = 36\,\mathrm{m/s}$ at $x = 9.94\,\mathrm{m}$.

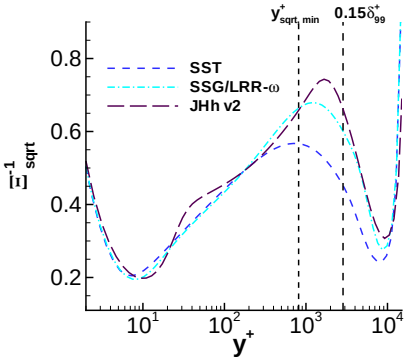

Figure 21. Question of high *Re* and the sqrt-law region.

CONCLUSIONS

The aim of this work was to isolate the effect of an adverse pressure gradient (APG) on the mean flow statistics of a turbulent boundary layer flow and to analyse history effects of mild convex curvature. The data support an empirical composite wall law with a log-law region above which a half-power law (or: sqrt-law) region forms. The wall law coefficients and the extent of the log-law region can be described as a function of the pressure gradient parameter. The experiment provides a large data-base for the validation of RANS turbulence models. The need for the direct measurement of the wall shear stress in regions of curved mean flow and significant pressure gradients was demonstrated. The comparison of RANS predictions with the experimental data shows the high accuracy requirements on the measurement data needed for a reliable improvement of RANS turbulence models.

ACKNOWLEDGEMENT

The experiment was funded in the DFG-project “Investigation of turbulent boundary layers with pressure gradient at high Reynolds numbers with high resolution multi camera techniques” (Grant KA 1808/14-1 & SCHR 1165/3-1) and by DLR AS.

REFERENCES

Alving, A. E., Smits, A. J. & Watmuff, J. H. 1990 Turbulent boundary layer relaxation from convex curvature. *Journal of Fluid Mechanics* **211**, 529–556.

Cecora, R.-D., Radespiel, R., Eisfeld, B. & Probst, A. 2015 Differential Reynolds-Stress Modeling for Aeronautics. *AIAA Journal* **53**, 739–755.

Gibson, M. M., Verriopoulos, C. A. & Vlachos, N. S. 1984 Turbulent boundary layer on a mildly curved convex surface. *Experiments in Fluids* **2**, 17–24.

Gungor, A. G., Maciel, Y., Simens, M. P. & Soria, J. 2016 Scaling and statistics of large-defect adverse pressure gradient turbulent boundary layer. *International Journal of Heat and Fluid Flow* **59**, 109–124.

Kähler, C. J., Scharnowski, S. & Cierpka, C. 2012 On the uncertainty of digital PIV and PTV near walls. *Experiments in Fluids* **52**, 1641–1656.

Kitsios, V., Atkinson, C., Sillero, J. A., Borell, G., Gungor, A. G., Jimenez, J. & Soria, J. 2016 Direct numerical simulation of a self-similar adverse pressure gradient turbulent boundary layer. *International Journal of Heat and Fluid Flow* **61**, 129–136.

Knopp, T., Buchmann, N. A., Schanz, D., Eisfeld, B., Cierpka, C., Hain, R., Schröder, A. & Kähler, C. J. 2015 Investigation of scaling laws in a turbulent boundary layer flow with adverse pressure gradient using PIV. *Journal of Turbulence* **16**, 250–272.

Knopp, T. & Reuther, N. 2015 A wall-law for adverse pressure gradient flows and modification for *k-ω* models. In *17th STAB workshop, 10th - 11th Nov. 2015, Göttingen*.

Nagib, H. M. & Chauhan, K. A. 2008 Variations of von Karman coefficient in canonical flows. *Physics of Fluids* **20**, 101518–1–10.

Nickels, T. B. 2004 Inner scaling for wall-bounded flows subject to large pressure gradients. *Journal of Fluid Mechanics* **521**, 217–239.

Novara, M., Schanz, D., Reuther, N., Kähler, C. J. & Schröder, A. 2016 Lagrangian 3D particle tracking in high-speed flows: Shake-The-Box for multi-pulse systems. *Experiments in Fluids* **57**, 128 1–20.

Perry, A. E. 1966 Turbulent boundary layers in decreasing adverse presssure gradients. *Journal of Fluid Mechanics* **25**, 481–506.

Ramaprian, B. R. & Shivaprasad, B. G. 1978 The structure of turbulent boundary layers along mildly curved surfaces. *Journal of Fluid Mechanics* **85**, 273–303.

Reuther, N., Scharnowski, S., Hain, R., Schanz, D., Schröder, A. & Kähler, C. J. 2015 Experimental investigation of adverse pressure gradient turbulent boundary layers by means of large-scale PIV. In *11th International Symposium on Particle Image Velocimetry - PIV15, Santa Barbara, California, September 14-16, 2015*.

Schülein, E., Reuther, N. & Knopp, T. 2017 Optical skin friction measurements in a turbulent boundary layer with pressure gradient. In *New Results in Numerical and Experimental Fluid Mechanics. Contributions to the 20th STAB/DGLR Symposium Braunschweig, Germany 2016*.

Siliero, J. A., Jimenez, J. & Moser, R. D. 2013 One-point statistics for turbulent wall-bounded flows at reynolds numbers up to $\delta^+ \approx$ 2000. *Physics of Fluids* **25**, 105102–1.

Wilcox, D. C. 1998 *Turbulence modeling for CFD*. La Canada: DWC Industries.